8-24-2020

Deciphering tip-enhanced Raman imaging of carbon nanotubes with deep learning neural networks.

Usant Kajendirarajah

María Olivia Avilés

François Lagugné-Labarthet

ARTICLE

Deciphering Tip-Enhanced Raman Imaging of Carbon Nanotubes with Deep Learning Neural Networks

Received 00th January 20xx,
Accepted 00th January 20xx

DOI: 10.1039/x0xx00000x

Usant Kajendirarajah[a], María Olivia Avilés[a] and François Lagugné-labarthet[a,*]

Recent release of open-source machine learning libraries present opportunities to unify machine learning with nanoscale research, thus improving effectiveness of research methods and characterization protocols. This paper outlines and demonstrates the effectiveness of such a synergy with artificial neural networks to provide for an accelerated and enhanced characterization of individual carbon nanotubes deposited over a surface. Our algorithms provide a rapid diagnosis and analysis of tip-enhanced Raman spectroscopy mappings and the results show an improved spectral assignment of spectral features and spatial contrast of the collected images. Using several examples, we demonstrate the robustness and versatility of our deep learning neural network models. We highlight the use of machine learning and data science in tandem with tip-enhanced Raman spectroscopy technique enables a fast and accurate understanding of experimental data, thus leading to a powerful and comprehensive imaging analysis applied to spectroscopic measurements.

Introduction

Tip-enhanced Raman spectroscopy (TERS) provides an invaluable understanding of chemical processes and molecular organization at a nanoscale level and has facilitated advances in the fields of surface chemistry, as well as in nanomaterials and biomaterials.[1, 2] However, this technique has not yet achieved its full potential for rapid nanoscale chemical and structural analysis.[3] In particular, common spectral analysis methods are insufficient as they often exploit a limited portion of the several thousands of spectra collected during a TERS mapping experiment.[4]

TERS combines Raman spectroscopy and scanning probe microscopy and has become of great importance in material and biomaterial analysis, due to its spatial resolution routinely better than 20 nm and with some examples where resolution is even below 1 nm in ambient conditions.[5-9] TERS 2D mapping allows for acquisition of thousands of Raman spectra forming the hyperspectral cube within a single experiment, resulting in a tremendous amount of raw data to be gathered.[10]

The analysis of TERS maps is generally performed using variation of intensity of an integrated spectral range which reveals the spatial distribution of a specific vibrational mode using all the spectra or selected representative spectra. Another frequently used spectroscopy data analysis method is principal component analysis (PCA), a dimensionality reduction algorithm that attempts to categorize and differentiate specific properties of analytes.[4, 11, 12] However, PCA poses limitations as the effectiveness is reduced with the presence of background or other spectral artefacts which can interfere with variance calculations.[4] Error rates in classification can be as high as 14% even with correction algorithms applied to the raw collected data. [4]

On the other hand, machine learning has shown efficacy in overcoming the limitations of these traditional data analysis methods. Machine learning uses statistical and mathematical models to gain inference of patterns in the data set.[13] Deep learning, a subset of machine learning, uses artificial neural networks (ANNs) as its primary machine learning method. ANNs are loosely based on information processing and communication nodes of biological systems, and can be categorized into supervised, unsupervised, or reinforcement learning. Herein, we used supervised learning, a term that encompasses tasks where machine learning models learn a mathematical function to map an input to an output based on labelled example input-output pairs (the training dataset). Once an inferred function has been produced, it is then used to map new and unseen examples of experimental data. Optimization of machine learning models is important as it allows to circumvent outliers without compromising accuracy in discrimination of expected instances, a drastic improvement to PCA. For example, in the case of TERS data, anomalies such as cosmic rays must still be identified accurately which we demonstrate with our ANNs. In addition, machine learning allows for high precision diagnosis of collected TERS data without having the need for initial treatment applied to the raw data.

Examples of applications of machine learning to chemistry are found in quantum chemistry,[14] predicting viscosity of multi-walled carbon nanotubes using ANNs,[15] and thermodynamics of biochemical redox reactions.[16] Previous work of machine learning applications to analyse Raman spectroscopy has shown

[a] *The University of Western Ontario (Western University), 1151 Richmond Street, London, On, N6A 5B7, Canada.*

Electronic Supplementary Information (ESI) available: [details of any supplementary information available should be included here]. See DOI: 10.1039/x0xx00000x

improvement of brain cancer detection,[9, 17] and surface-enhanced Raman spectra assignment of multiplexed metabolites in different cell lines.[18] Additionally, applications in forensics, food and beverages, and medical diagnostics have been reported to combine Raman with deep learning, suggesting the prevalence and adaptability of machine learning.[19]

In this work, TERS maps were measured on single-walled carbon nanotubes (SWNTs), a well-studied material which serves here as a reference nanoscale object.[1, 5, 20 21] TERS spatial resolution together with spectral selectivity is used to facilitate discrimination of semiconductive versus metallic characteristics of SWNTs,[22-24] the identification of bundles,[25-27] and the identification of defect areas.[28, 29] Machine learning applications to TERS data have yet to be explored and we demonstrate that machine learning provides for an unprecedented opportunity to treat collected TERS data with more confidence.

In particular, we outline the creation and utilization of two multi-purpose ANNs to characterize SWNTs. Using Raman spectra gathered from TERS experiments, ANN Model 1 classifies each spectrum as background or carbon nanotube with an associated confidence percentage. ANN Model 2 provides clear and rapid filtering of the three vibrational modes of carbon nanotubes. For any given carbon nanotube Raman spectrum, ANN Model 2 accurately identifies the existence of these modes. Both ANN Model 1 and Model 2 are used to generate TERS maps with enhanced contrast. ANN Model 1 and ANN Model 2 work synergistically to identify the number and the assignments associated with the different SWCNTs vibrational modes. In addition, the developed approach enables enhanced visualization of carbon nanotube defect areas.

Our methodologies used to create our deep learning ANNs have resulted in a 98 % accuracy for ANN Model 1 and 96 % accuracy for ANN Model 2. Our approach performs a diagnosis of unseen raw TERS hyperspectral data in only 4 to 6 hours for a spectral cube composed of 8000-10000 set of spectra with 1600 points each. We show the robustness of our neural networks as sensitivity and performance is maintained when used on carbon nanotubes of differing diameters and regardless of their metallic or semiconductive character. All discoveries we outline in this paper have not yet been accomplished and are not possible with currently existing software tools.

Experimental

Samples. Single walled carbon nanotubes with 0.03 mg/mL (Nanointegris Isonanotubes-M 99% Solution) were drop-casted as received onto a template stripped gold substrate. These metallic SWNTs varied in diameter between 1.2-1.7 nm. Additionally, SWNT (Nanointegris HiPco purified) was purchased and prepared with 0.5 mg/mL in 1 % sodium dodecyl sulfate (SDS), sonicated for 1 hour and 20 minutes, and then centrifuged for 1 hour at 1500 rpm. The semiconductive SWNTs were drop-casted as prepared into a template stripped gold substrate. After 24 hours of drying, to remove the surfactant, water with acetic acid (0.1 % v/v) was used to rinse the substrate with SWNTs.

TERS Experiment. All TERS experiments were accomplished using an OmegaScope atomic force microscope combined to an XploRa Raman microspectrometer (HORIBA Scientific) equipped with a 600 grooves/mm grating, pictured in Fig. S1. The laser power was set to 0.25 mW at the sample and focused with a 100X objective with 0.7 of numerical aperture (N.A.) in reflection geometry. These parameters together with an acquisition time of 400 milliseconds per pixel were selected to keep the integrity of the carbon nanotube, avoid scanning drift, and to not compromise the tip's apex with increased laser power. OMNI TERS NC probes coated with 60 nm of Au, spring constant of 93 N/m, and a resonance frequency of 320 kHz were used. These tips were used to acquire the maps in conjunction with 638 nm excitation wavelength. Optical scattering was first performed to identify a hotspot at the apex of the tip for TERS enhancement. An AFM scan was obtained first through setting an oscillation amplitude of ~20 nm. An area of (100× 100) pixels was selected representing 10000 Raman spectra to be recorded. Tapping mode was used for AFM with a scanning rate of 1 Hz. For the TERS point measurements, the tip is brought in contact with the sample and the applied force of the tip on the sample was tuned in order to obtain the highest TERS intensity through the Nfshift parameter specific to this instrument. IAPro and Gwyddion software applications were used for processing of the AFM and TERS maps.

Machine Learning. Packages from the Python (version 3.7.3) data science software stack were used in the data pre-processing and feature engineering stages of the machine learning workflow and are as follows: Pandas version 0.25.0, Matplotlib version 3.1.1, and NumPy version 1.17.0. Together these software tools allowed for data manipulation, data analytics, and data mining with ease. Standardized definitions of the terminology used in machine learning and outlined in this paper are summarized in Table 1.

The construction of the architecture and topology of our ANNs as well as training occurred in Jupyter Notebook. Seaborn version 0.9.0 was used to create heat-maps and assess the correlation of native and derived features of the data set. We used Keras version 2.2.4 with Google's free open-source deep learning library TensorFlow version 1.14.0 as the backend for our ANNs. TensorBoard version 2.1.0 was used to monitor and assess accuracy and loss functions for our ANNs and can be found in Fig. S2. Once accuracy and loss functions showed optimization, the configurations of our ANNs were then exported from Jupyter Notebook in JSON or YAML format to be imported and incorporated into our software. Our software reads large quantities of raw TERS hyperspectral mapping data as input and makes predictions using our machine learning models in order to create enhanced ANN-generated hyperspectral maps.

Table 1. Summary of standardized and useful terminology that is used in machine learning.

Term	Definition
Artificial neural network (ANN):	Machine learning model used in deep learning.
Independent features:	The features that are received by the input layer to be fed into the neurons.
Dependent features:	The features that are being predicted by the ANNs.
Hyperparameter:	A parameter whose value is set before learning process begins. Affects the speed and quality of the learning process. Examples include topology, architecture, and size of neural network.
Sigmoid activation function:	A mathematical function used in the output layer to normalize the output (prediction) as 0 or 1, which correlates to and eases classification.
'ReLU' activation function:	Most commonly used mathematical function in the nodes of hidden layer of neural networks.
Epochs:	Number of passes through the entire training dataset the machine learning algorithm has completed.
Batch size:	The number of samples that will be propagated through the neural network.

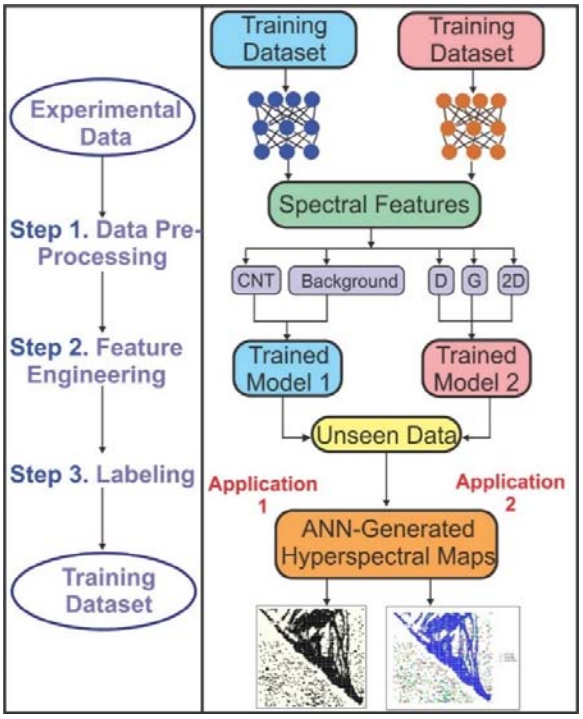

Fig. 1 Machine learning workflow. The necessary steps taken to achieve the efficacy of ANN models and generate ANN-generated hyperspectral maps. Spectral features (CNT or background) are identified by ANN Model 1. ANN Model 2 identifies existence of spectral features (D, G, 2D bands).

Dealing with large amounts of data can be resource demanding and local hardware may not suffice to the task. As a result, cloud computing allowed to overcome this bottleneck. A virtual instance in Google Cloud Computing (n1-highcpu-16 16vCPUS, 14.4 GB RAM) was used to process the extensive amounts of experimental data and train the neural networks with ease. With these specifications, processing an entire hyperspectral cube of 10000 TERS spectra (approximately 16 million points of information) is done in 4 to 6 hours.

Results

Machine Learning Workflow

The machine learning workflow applied to TERS is summarized in Fig.1. This process is iterative at multiple levels and requires necessary revisiting and tweaking in order to achieve optimized machine learning models. For example, data pre-processing and feature engineering are data analysis and mining techniques that may require several iterations in order to improve optimization. As well, selection of an appropriate machine learning method (supervised learning, deep learning ANNs in our case), architecture and topology of ANNs, and hyperparameter optimization play their respective roles of equal importance in achieving optimized results. Herein, we outline the specific steps taken that led to the accuracy and efficacy of our data analysis. TERS experiments were performed on semiconductive and metallic SWNTs, which we hereby refer as CNT1-semi and CNT2-metal, respectively.

Additional examples of semiconductive carbon nanotubes are represented in Figs.S3, S4 and are referred to as CNT3-semi and CNT4-semi. To transform experimental data into the training dataset, three steps were taken and are as follows: Step 1 (data pre-processing), Step 2 (feature engineering), and Step 3 (labelling). These three steps are outlined in detail below.

STEP 1: Data pre-processing — Data pre-processing is essential to discard superfluous data to avoid convoluting our ANNs with unnecessary information and patterns that can impact learning. We pre-processed the experimental data by focusing only on the Raman wavenumbers intervals at which lies the crucial information. Data outside of these relevant spectral portions do not add any additional value to the decision-making of our machine learning models. In the case of ANN Model 1, the determination of the existence of a primary G vibrational band is sufficient to distinguish between carbon nanotube and background. Similarly, for ANN Model 2, we only focus on the three regions key vibrational features are found: 1234-1368 cm^{-1} for the D band, 1458-1651 cm^{-1} for the G band, and 2450-2750 cm^{-1} for the 2D (G') band. Hence, we have only used the relevant spectral portions of the spectra to significantly narrow the focus of our dataset. Furthermore, our training data set derives as a subset from the larger 10000 obtained TERS spectra of CNT2-metal. For the broader set of 10000 TERS spectra, we analysed intensity characteristics such as quartiles, standard deviation, variance, mean, and median in order to strategically select a subset of 75 TERS spectra (of which 30 pertains to background, and 45 pertains to SWNT) as the best candidates to wholly reflect the chemical information in our training dataset. This

partition and number of spectra were chosen because it gave satisfactory convergence and worked best with the chosen hyperparameters. The remaining 9925 spectra of CNT2-metal and all spectra of CNT1-semi, CNT3-semi, and CNT4-semi are considered unseen novel data. Pandas, Matplotlib, and NumPy mentioned in the experimental and methods section were used to accomplish this data pre-processing.

STEP 2: Feature Engineering — Once the dataset has been pre-processed, feature engineering was applied to the dataset to improve decision-making of our machine learning models. Feature engineering allowed for us to extract additional features, via data mining techniques. Specific to our TERS experiments, the native (primary) features garnered from experimentation were only Raman shift and intensity, and these two alone were not sufficient to create effective ANNs. Therefore, we designed and derived secondary features to better expose and capture subtle and hidden patterns in the data to enhance decision-making. For ANN Model 1, we created secondary features to capture information examining the slope associated with the Raman mode, magnitude of peak, and rate of change in intensity as Raman shift increases leftmost to rightmost from 1458 to 1651 cm^{-1} (G mode range). By doing so, these features helped to exploit the distinctive differences in characteristics of background and SWNT Raman spectra. For example, between 1458 to 1651 cm^{-1}, a SWNT Raman spectrum will generally have a sharp incline and decline (a distinct inflection point indicating change in sign of slope). In addition, a sharper spectral feature will have a steeper slope because the peak is narrower. Furthermore, the magnitude of the peak in the G mode region will generally be greater in SWNT spectra. Rate of change in intensity allows to capture information regarding the general shape of the spectrum. In the case of SWNT spectra, this means an inverse parabolic shape at the G mode. Additionally, the background spectra show a downward hill shape. In terms of ANN Model 2, similar logic applies. In addition, ANN Model 2 used two additional secondary features to help distinguish between SWNT and background Raman spectra, and thus ANN Model 2's performance is closely dependent on ANN Model 1's. As a result, together we have five independent features (Raman shift, Raman intensity, slope, magnitude of the peak, and rate of change in intensity) for ANN Model 1 and seven independent features (Raman shift, Raman intensity, slope, magnitude of the peak, rate of change in intensity, identifier for CNT, and identifier for background) for ANN Model 2. Pandas, Matplotlib, and NumPy were used for this step.

STEP 3: Labelling — Once feature engineering has been completed, the final step is to label the dataset. For this, we used a strategy called one-hot encodings to represent our categorical data as unit vectors. In the case of ANN Model 1, 'background' was labelled and represented as [0 1] and carbon nanotube was labelled and represented as [1 0]. Likewise, for ANN Model 2, the vectors [0 0 0 1], [0 0 1 0], [0 1 0 0], and [1 0 0 0] represented 'Noise', 'D-Band', 'G-Band', and '2D-Band' respectively. The advantage of such a strategy is that it is easy to design and modify and output can only belong to defined categories. The disadvantage is that because states can only belong to designated unit vectors, a neural network model with greater number of labels can waver in computing performance as labels becomes cumbersome.

With these three steps completed, the experimental data has been successfully transformed into the training dataset and is now ready to be used by the ANNs. The architecture of the neural network is outlined as follows. ANN Model 1 classifies spectra as carbon nanotube or background and decision-making depends on the existence or lack of a primary mode G band. As a result, one singular ANN is responsible for this binary classification.

ANN Model 2 is responsible for identifying the existence of three vibrational features, so therefore ANN Model 2 is an amalgamation of three independent ANNs, of which each constituent is responsible for classifying a specific vibrational mode. For example, ANN Model 2 constituent 1 assesses the likelihood of the existence of the D band at the D band range only and classifies accordingly. Likewise, ANN Model 2 constituent 2 and constituent 3 perform similarly for the G and 2D (G') band respectively. The architecture of the ANNs can be split into three components: the input layer, the hidden layer, and the output layer. The input layer receives the number of independent features (Raman shift, Raman intensity, slope,…) that are fed into the neurons. As mentioned previously, ANN Model 1 has five and ANN Model 2 has seven independent features. The hidden layer is composed of neurons responsible for the mathematical computations. In the case of ANN Model 1 and Model 2, all abstractions have two hidden layers of 20 neurons each. The output layer uses a sigmoid activation function to normalize the output as a 0 or 1, which correlates to our dependent features, the values being predicted. In the case of ANN Model 1, this is 'background' or 'carbon nanotube'. In the case of ANN Model 2, this is 'Noise' or 'D-Band' for the first constituent, 'Noise' or 'G-Band' for the second constituent, and 'Noise' or '2D-Band' for the third constituent.

Hyperparameters are parameters whose value is set before the learning process begins. Hyperparameters include the ratio of the splitting of the training data set, number of neurons at each hidden layer, number of hidden layers of each ANN, and activation functions used. Hyperparameter optimization is important to achieve optimal results, as inefficient hyperparameter selections can result in overfitting or underfitting. Overfitting results from overtraining and essentially means the ANNs will have memorized the data set and may therefore fail to fit any additional data or predict future observations reliably. Similarly, underfitting results from undertraining and means the statistical models are unable to adequately detect and capture the underlying structure of the training data set, resulting in lower performance. It is important to find the optimal ratio to split the training data into training and validation sets as inefficient splitting can result in overtraining or undertraining. In the case of our ANNs, we achieved optimal results by splitting the training data set as 70% training and 30% validation. We used the rectified linear unit 'ReLU' activation function for our hidden layers and as mentioned previously a sigmoid activation function for the output layers. In addition, another hyperparameter includes layer type and we used 'Dense' layers. Dense layers allow for each neuron to receive input from all neurons of the previous layer. Hyperparameters during training process include epochs, which is the number of passes through the entire training dataset the machine learning algorithm has completed, and batch size. For our ANNs Model 1 and Model 2, we used 100 epochs with a batch size of 500 for all abstractions. Together, these hyperparameters were all viable for adjustments in order to improve the efficacy of the achieved ANNs.

Once the models have been constructed and trained, our ANNs were used to make predictions on unseen TERS data to assess accuracy of real applications. The workflow described in steps 1 and 2 and in the hyperparameter optimization was adjusted if needed to improve the accuracy of the predictions. This continuing process came to a halt as real application accuracies of 98% for Model 1 and 96% for Model 2 were achieved. Code for the architecture of our ANN Model 1 and ANN Model 2 can be found on GitHub as indicated in the supporting information section. As Fig.1 suggests, these models were then used to create our enhanced ANN-generated hyperspectral maps.

Applying ANN Models to Predict Raman Spectra Properties.

Fig.2 shows the capabilities of our ANN models by demonstrating predictions on unseen TERS data belonging to CNT2-metal. As mentioned before, ANN Model 1 is responsible for identifying a spectrum as 'CNT' or 'Background' with an associated percentage to reflect confidence in classification. Figures 2A-D show spectra classified as CNT. Figures 2A, 2C, and 2D have a prediction confidence of 100% and this is due to a clear-cut existence of the primary G band. Fig.2B is classified as CNT with 75.5% and this slightly lower percentage may be attributed to the surrounding noise which may be a result of the background. Fig.2E shows a TERS spectrum identified as 'Background' with a percentage of 54.7% because of the presence of a G mode with weak intensity.

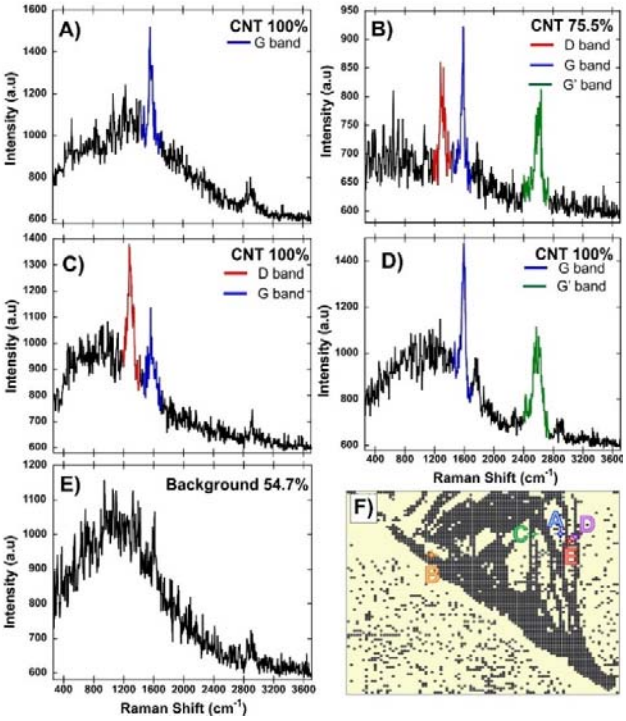

Fig. 2 ANN Model 1 and ANN Model 2 applied to unseen Raman spectra obtained from TERS experiment for CNT2-metal. A) CNT identification with 100% confidence. Only G band present. B) CNT identification with 75.5% confidence. D, G and 2D(G') bands present C) CNT with 100%. Only D and G bands are present. D) CNT with 100% confidence. Only G and G' band are present. E) background with 54.7% confidence. no bands present F) ANN-generated hyperspectral map of CNT2-metal shows the locations where Raman spectra A-E were acquired.

ANN Model 2 is responsible for identifying the number of and combination of vibrational bands. In this work, we focus only on the identification of the three main vibrational bands: D, G and 2D (interchangeably G'). As shown, Fig.2A-D show all possible combinations (G only, D and G and G', D and G' only, or G and G' only). Fig.2F is an ANN-generated hyperspectral mapping with enhanced contrast provided by ANN Model 1. In this figure, each Raman spectrum with features similar to Figures 2A-D are correlated to the X, Y coordinate of the hyperspectral map and pinpointed by a black pixel. The background spectra (Fig.2E) appear as a yellow homogeneous color in Fig.2F. Furthermore, maximum Intensity ($I_{\max}$) values of each band is able to be extracted and is highlighted in the ANN-generated defect density distribution hyperspectral map that is discussed later.

Fig.2A exposes the carbon nanotube spectrum in a specific position in which there exists the G band only. The classification result in this case identifies one peak only that can be associated to an allotrope carbon debris. Additionally, another band is revealed around 2900 cm^{-1} which corresponds to the C-H vibration.[30] The observation of C-H band in Figures 2A, 2C, and 2E is generally indicative of a surfactant residue that could be located in or out the carbon nanotube. A new band appears in Fig.2D in the range of 1700-1900 cm^{-1}, which may be identified as the iTOLA mode. The iTOLA band occurs due to the combination of in-plane transverse optical phonon and the longitudinal acoustic (LA) phonon when electronic resonance conditions are met.[31]

Experimental Spatial Resolution of TERS.

The topography and the TERS maps of the G mode of a bundle of carbon nanotubes that splits into several smaller bundles are shown in Figs. 3A and 3B, respectively. The cross sections displayed in Fig.3A are indicated on different area of the sample and are indicative of the lateral topographical resolution of our AFM instrument which is convoluted by the tip geometry. These values are larger than the Z values which provides a more precise assessment of the diameter of the bundles. The cross sections 1-6 are reported in Fig.3C-F. The lateral measurements based on the full width at half height varies from 21 to 77 nm (Fig.3 C-F), meanwhile the height of the carbon nanotubes bundles varies from 1 to 10 nm (Fig.3C, E). Interestingly, the TERS images based on the integration of the G mode (Fig.3B) shows cross sections that are sharper than the topographical images due to the localized EM confinement at the tip extremity. Based on the smaller nanotube bundle measured, the estimated spatial resolution of these TERS measurements are about ~25 nm, a value that is limited by the tip geometry and smooth coating used in this experiment. Although this is beyond the scope of this manuscript, higher spatial resolution can be obtained with rougher coating creating single metal nanoparticle at the extremity of the probe.[32] Moreover, two more bundled carbon nanotubes maps can be found in the supporting information Figs. S5, S6, revealing a lateral resolution of ~16 nm. A different sample (CNT2-metal) was also investigated and the associated AFM and TERS images and cross sections are provided in Fig.S7.

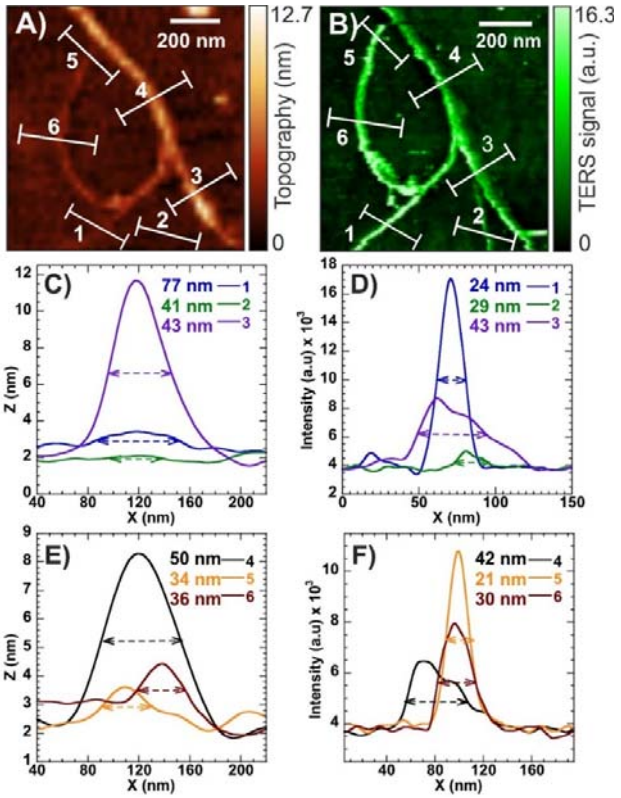

Fig. 3 A) AFM height profile scan of the CNT1-semi. B) TERS map shows the Intensity of the G band CNT1-semi. C) Cross sections 1-3 of the height profiles. D) Cross section 1-3 of the TERS intensity profile. E) Cross sections 4-6 of the height profiles. F) Cross section 4-6 of the TERS intensity

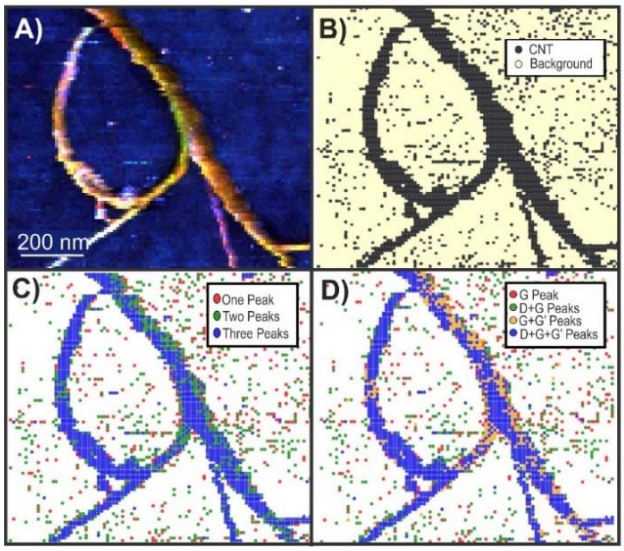

Fig. 4 A) All color TERS map of CNT1-semi. B) ANN Model 1 map discriminating background versus CNT spectra. C) ANN Model 1+2 map classifying the spectra by number of peaks present. D) ANN model 1+2 map classifying the spectra into four different viable classes of peaks present.

Chemical Analysis of ANN-Generated Hyperspectral Maps.

Fig.4A shows an all color TERS map. Each vibrational band is represented in blue, green and red for D, G and G', respectively, and is integrated as one single map to generate this all colored TERS map. The higher brightness white color seen in Fig.4A represents the combined similar (or equal) intensity of the three bands together. Figures 4B-D show newly ANN-generated hyperspectral maps that were created using ANN Model 1 alone (Fig.4B) and ANN Model 1+ANN Model 2 (Fig. 4C, D). Fig.4B is an ANN-generated hyperspectral mapping with increased contrast in TERS imaging. Fig.4C reveals the number of vibrational bands present at each carbon allotrope with a set of (X,Y) coordinates. As shown in Fig.4C, the possible number of vibrational bands corresponds to one peak, two peaks, or three peaks observed. The high dispersion of the vibrational signals of carbon material present in the background is indicative of small debris of carbon allotropes that were not identifiable in the TERS image in Fig.4A. Figures 4D goes one step further and segregates the classifications into specific peaks observed. Four classes exist now as the former two peaks class of Fig.4C becomes two separate subclasses. The composition breakdown is categorized as only G (one peak), only D and G (two peaks), only G and G' (two peaks), or D and G and G' (three peaks). As a result, these two figures can give a comprehensive understanding of the total band composition that appears at each specific X,Y coordinate of the hyperspectral map. With this new information, this allows for rapid diagnosis and chemical analysis of CNT1-semi's structure.

In Fig.4D, the green pixels reveal an absence of the G' band and are mainly present outside the carbon nanotubes. This lack of G' band may be attributed to the oxidation of the allotrope carbon debris. Furthermore, Fig.4D suggests that there is a higher density of the G+G' bands (orange pixels) appearing at the sides of CNT1-semi bundles, revealing the absence of the D band in these particular regions and subsequently less defects in these regions. The latter agrees with Fig.S8 representing the variation of TERS intensity of each of the modes and their superimposition. The maps show a decrease of the D mode TERS signal intensity in these same areas. In SWCNTs, the D band intensity is affected by a complex interplay of electronic resonances and chirality-dependent electron-phonon coupling.[33]

The blue pixels in Fig.4C, D represent locations where all three vibrational modes are present and are consistent with the characteristic vibrational spectra of SWNT. The blue pixels found sparsely outside the nanotubes may be associated to residues as a result of sonication.

The same observations above apply to Fig.5, an analysis of CNT2-metal's structure. Fig.5A shows the TERS image of carbon nanotubes ripped into various threads. From the TERS map, Fig.S9 shows the independent integrations for the D, G and G' bands of CNT2-metal that are superimposed in an all-color map. Fig.5B is generated using ANN Model 1 to discriminate background from carbon-containing material. Figures 5C, D show the presence of the three bands along the carbon nanotube as evidenced by the distribution of blue pixels. Isolated pixels close to the SWNT vertical threads are indicative of D+G modes (green pixels) as highlighted in Fig.5D and are presumably due to the presence of oxidized sites.[34]

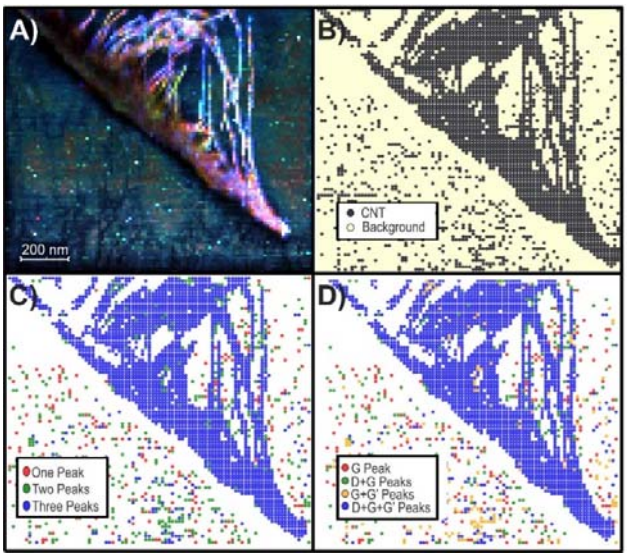

Fig. 5 A) All color TERS map of CNT2-metal. B) ANN Model 1 map discriminating background versus CNT spectra. C) ANN Model 1+2 map classifying the spectra by number of peaks present. D) ANN model 1+2 map classifying the spectra into four different viable classes of peaks present.

Fig. S10 highlights better the distribution of these oxidized states for all the samples studied in this work. Additionally, for samples CNT1-semi and CNT2-metal, Fig. S11 shows selected corresponding Raman spectra of isolated pixels in the background that show CNT-like character. These results demonstrate the versatility and sensitivity of our ANNs to identifying differing spectra including in the background where these spectra are often discarded.

Characterizing Semiconductive and Metallic Carbon Nanotubes.

Independent TERS mapping was performed to identify the spectral differences of two different types of carbon nanotubes. TERS maps of CNT1-semi and CNT2-metal highlight the structural split and shift of the G mode as shown in Fig.6 where the G band splits into G^+ and G^- bands. Low laser power and short acquisition time were critical parameters in analysing metallic SWNTs, since an increase in the power may generate an irreversible change in G band therefore affecting the metallic or semiconductive character.[35]

TERS maps of semiconductive and metallic CNTs are shown in Fig.6A, B, respectively. The semiconductive TERS spectra can be observed in Fig.6C selected from averaged locations (Fig.6A) of CNT1-semi. Similarly, selected spectra of CNT2-metal are shown in Fig.6D. Fig 6C,D highlight a clear shift and broadening of the G- band.

It was previously reported that the origin of the G^+ and G^- modes is associated with longitudinal-optical (LO) and transverse optical (TO) phonons.[24, 36] In metallic nanotubes specifically the

LO phonon results in a broader band (Fig.6D) where the G- and the G+ have almost the same intensity and are difficult to separate.[24, 37]

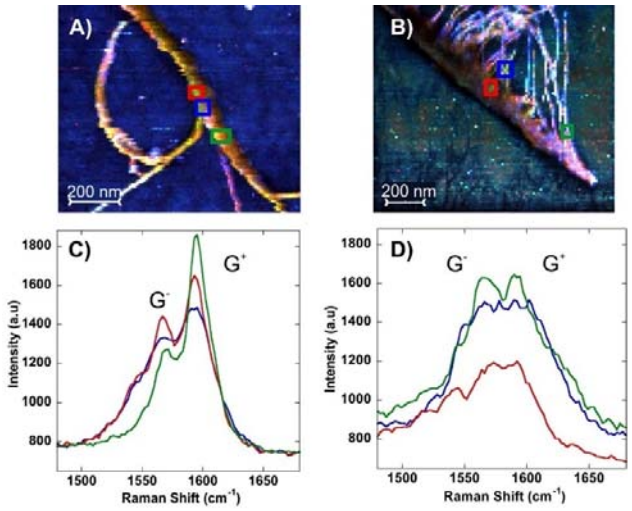

Fig. 6 A) TERS all colored map showing the selected averaged areas for CNT1-semi. B) TERS all colored map showing the selected averaged areas for CNT2-metal. C) Averaged spectra for each of the locations selected for CNT1-semi. D) Averaged spectra for each of the locations selected for CNT2-metal.

Given the inhomogeneous distribution of such proximity in G- and G+ intensities, some areas are presumably semiconductive as shown in the red spectrum displayed in Fig.6D. Regardless of the conductivity nature of the carbon nanotubes bundles, our ANN Models do not decline in performance. This approach could be applied to mixtures of metallic and semiconductive CNTs and revealing their interactions and distribution at surfaces.

Enhanced ANN-Generated Defects Density Distribution Hyperspectral Mapping

TERS imaging allows for gaining insight of defect areas and correlating these areas to the geometry form of the carbon nanotubes. CNT1-semi and CNT2-metal contain high density of defects in certain areas. Defects in carbon nanotubes can be produced in the synthesis process, be induced during the sample preparation, or induced by the scanning tip. We investigate the correlation of the bundles and bending of the carbon nanotubes, which in turn generate an increase of the D band response in affected areas. Fig.7 shows the defect analysis of CNT1-semi and CNT2-metal. Specifically, Fig.7A and Fig.7B are extracted from the TERS images and represent the ratio of intensities of the D and G modes, I_D/I_G, for CNT1-semi and CNT2-metal, respectively. These two maps therefore represent the spatial distribution of defects of the two samples. Figures 7C and 7D are ANN-generated hyperspectral maps that provide a better discrimination of defects from the background, highlighting the presence of debris around the main bundles. In these maps, the I_D/I_G ratios are more precise as these values are extracted directly from ANN Model 2 alone, because the algorithm takes into consideration only the "CNT" classified spectra instead of all the spectra from the raw TERS data. As a result, these new maps give higher spatial resolution regarding the defect density distribution. On the contrary, the raw TERS maps shown in Figures 7A, B show defect distributions when I_D/I_G is taken for all spectra regardless of background or CNT. This provides a good estimate of where defects are largely localized but it is not accurate as background spectra are included in the calculation. Results suggest that CNT2-metal has a greater defect factor of $I_D/I_G = 3.4$ versus 2.5 for CNT1-semi as shown in Figures 7A, B. As a result of our algorithms, Figures 7C, D obtained from our ANNs suggest that CNT2-metal has a greater defect factor of $I_D/I_G = 4.3$ versus 2.7 for CNT1-semi, and this allows for better visualization.

Specifically, CNT2-metal has many bundled threads of carbon nanotubes that have been mechanically ripped during the scanning TERS measurement, resulting in a higher defect factor. Figures 7B shows a higher density of defects, highlighted by the darker orange regions localized on the bundles. For CNT1-semi, similar observations can be made with additional presence of defects at the curvature of the bent bundles. From the maps (Fig.7A, B) averaged areas were selected to analyse the TERS spectra in different locations. The spectra from the selected red, blue and black areas in Fig.7A, B are shown in Figures 7E, F with the corresponding colors. Fig.7F reveals several peaks (splitting) within the D band of CNT2-metal. The latter may be attributed to the double resonance theory which has been previously reported.[38] The double resonance is associated to an elastic scattering of the phonons around the K and Γ point of the graphite Brillouin zone.[31]

Discussion

As demonstrated, results show the applicability of machine learning to achieve an enhanced TERS analysis of carbon nanotubes with an accuracy of 98% for ANN Model 1, and an accuracy of 96% for ANN Model 2. To summarize, ANN Model 1 is responsible for classifying each TERS spectrum as background or carbon nanotube with an associated confidence percentage. ANN Model 2 is responsible for classifying the three vibrational bands of carbon nanotubes provided that the D, G, and G' bands are present. Note that ANN Model 2's predictions are dependent on ANN Model 1's predictions and this means that error rates compound, i.e. applying twice an ANN with a 98% accuracy yields a resulting accuracy of 96%. This explains the slight decrease in accuracy for ANN Model 2. The unification of the two ANNs and our machine learning approach provide for a rapid, accurate and comprehensive analysis of raw TERS experimental data.

High spatial resolution is revealed for all carbon nanotubes samples presented in this TERS-Machine learning study. In addition to the TERS experiments that provide an enhanced spatial resolution, ANN-generated spectral maps highlight the structural conformation of carbon nanotubes. The latter contributed in analysing the chemical properties of each of the carbon nanotubes, and such analysis included metallic or semiconductive classification and defect density determination.

It can be assumed that the present sample is a mixture of conformational zigzag and arm-chair structures of the SWNT bundles. According to our results, D band decreased in specific locations of the semiconductive SWNT bundle possibly due to electron-phonon coupling.

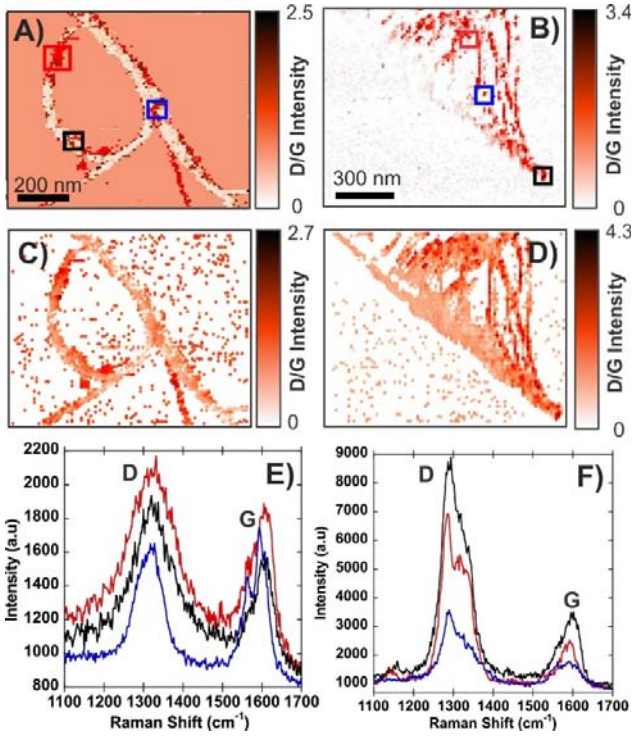

Fig. 7 A) I_D/I_G ratio intensity map of CNT1-semi obtained from the TERS maps. B) I_D/I_G ratio intensity map of CNT2-metal. C) ANN Model 1+2 map showing I_D/I_G ratio with more precise values for CNT1-semi. D) ANN Model 1+2 map showing I_D/I_G ratio with more precise values for CNT2-metal. E) TERS spectra for each of the average locations determined in A. F) TERS spectra for each of the average locations determined in B.

Through the TERS maps acquisition, CNT2-metal has a greater nfshift (force applied from the tip to the sample) and this was increased to generate defects and strains in the carbon nanotube for induced defect studies. This explains the rupture seen in CNT2-metal, showing a structural deformation of the bundles. Machine learning generated spectral mappings show debris of carbon allotrope that could also have formed during the scanning or sample preparation.

Further analysis of the ANN-generated hyperspectral maps shows a disappearance of D and G' bands which was observed in certain areas within or on the edges of the carbon nanotubes. The absence of the D band may be attributed to the defect-free conformal structure localized within the carbon nanotubes. The D vibrational band has been associated to in-plane vacancies, grain boundaries and strains.[5, 39] Furthermore, the absence of the D band has been associated to the excitation wavelength and possible oxidation of carbon nanotubes.[34] The disappearance of the G' band has also been reported and is presumably assigned to high oxidation during sample preparation.[34]

Additional vibrational modes that were not characteristic of carbon nanotubes were detected and correspond to C-H vibrations and the iTOLA band. Further investigation suggests these bands are due to surfactant organic residue from sample preparation (C-H mode) or a resonance condition.[30, 31] The iTOLA band appears due to the combination of optical and acoustic modes.[40] This band might appear due to the introduction of a much diluted acid treatment to remove some of the organic residue from the surfactant during sample preparation. The peak presence is important given that previous studies have reported the iTOLA band depends on the double resonance process which is dependent on the excitation wavelength.[31]

The spectral analysis of the G band that is further processed by our ANNs enables to classify the metallic or semiconductive character of the SWNTs with an excellent confidence.

Conclusions

We demonstrated a high spatial resolution tip-enhanced Raman mapping of 4 different bundles of carbon nanotubes, obtaining a spatial resolution of ~16 nm. Beyond the spatial resolution of this series of experiments, we developed two deep learning ANNs which yield a fast and enhanced TERS image analysis of carbon nanotubes. We described three ANN-generated hyperspectral maps for increased quality of imaging. The first ANN-generated hyperspectral map was responsible for giving an increased contrast by accurately segregating carbon nanotube spectra from background. The second ANN-generated hyperspectral map obtained showed the number of and composition of vibrational bands at each specific X, Y coordinate position. In addition, we described a third ANN-generated hyperspectral map that highlights a more precise defect density distribution information of carbon nanotubes based on the analysis of the I_D/I_G ratio. The obtained results are consistent with literature and demonstrate the value of an interdisciplinary synergy of machine learning, data science, and nanotechnology for TERS image analysis. These ANN models are therefore expected to be advantageous tools to facilitate the comprehensive understanding of garnered TERS experimental data with room for future extensions.

This collaborative effort is only in its infancy and there exists ample room for progression. For example, to study carbon nanotube conductivity, a future study we suggest is to create a deep learning ANN to classify on a given hyperspectral map the carbon allotropes as semiconductive or metallic. This conductivity information is revealed by the distinctive characteristics of the primary G vibrational band, and this classification can be done with similar methodologies to the ones outlined in this paper. Furthermore, artificial intelligence and machine learning have more to offer than the preliminary work and methods discussed in this paper. Classification, supervised learning, and deep learning with ANNs only scratch

the surface of the capabilities of machine learning. To name a few, concepts such as transfer learning, unsupervised learning techniques, clustering, and reinforcement learning are worth exploring. For example, unsupervised learning can be used to work with systems in which spectral features are not known. A neural network architecture specifically designed for clustering such as self-organizing maps can be used to tackle such a problem. These techniques can be integrated in order to build innovative solutions to tackle complex problems. It is only through this collaborative effort of multiple disciplines that it is possible for super-resolution microscopy techniques to make most use of data collected by instrumentation.

Conflicts of interest

There are no conflicts to declare.

Acknowledgements

This research was supported by the Natural Sciences and Engineering Research Council (NSERC) of Canada through a Strategic Partnership grant (STP 521543-18). The authors acknowledge Dr. Andrew Whitley (HORIBA Scientific) and Jefford Humes (NanoIntegris Technologies Inc.) for their valuable help to this project.

References

1. L. G. Cançado, A. Hartschuh and L. Novotny, *J. Raman Spectrosc.*, 2009, **40**, 1420-1426.
2. C. Blum, T. Schmid, L. Opilik, S. Weidmann, et al., *J. Raman Spectrosc.*, 2012, **43**, 1895-1904.
3. B. S. Yeo, J. Stadler, T. Schmid, R. Zenobi, et al., *Chem. Phys. Lett.*, 2009, **472**, 1-13.
4. G. Das, F. Gentile, M. L. Coluccio, A. M. Perri, et al., *J. Mol. Struct.*, 2011, **993**, 500-505.
5. N. Kazemi-Zanjani, P. Gobbo, Z. Zhu, M. S. Workentin, et al., *Can. J. Chem.*, 2014, **93**, 51-59.
6. D. N. Voylov, V. Bocharova, N. V. Lavrik, I. Vlassiouk, et al., *Nanoscale Adv.*, 2019, **1**, 3392-3399.
7. M. Nicklaus, C. Nauenheim, A. Krayev, V. Gavrilyuk, et al., *Rev. Sci. Instrum.*, 2012, **83**, 066102.
8. A. Bhattarai, I. V. Novikova and P. Z. El-Khoury, *J. Phys. Chem. B*, 2019, **123**, 27765-27769.
9. Z. He, Z. Han, M. Kizer, R. J. Linhardt, et al., *J. Am. Chem. Soc.*, 2019, **141**, 753-757.
10. M. Gühlke, Z. Heiner and J. Kneipp, *Phys. Chem. Chem. Phys.*, 2016, **18**, 14228-14233.
11. I. S. Patel, W. R. Premasiri, D. T. Moir and L. D. Ziegler, *J. Raman Spectrosc.*, 2008, **39**, 1660-1672.
12. R. Tantra, R. J. C. Brown and M. J. T. Milton, *J. Raman Spectrosc.*, 2007, **38**, 1469-1479.
13. Y. LeCun, Y. Bengio and G. Hinton, *Nature*, 2015, **521**, 436-444.
14. K. T. Schütt, M. Gastegger, A. Tkatchenko, K. R. Müller, et al., *Nat. Commun.*, 2019, **10**, 5024.
15. M. Afrand, A. Ahmadi Nadooshan, M. Hassani, H. Yarmand, et al., *Int. Commun. Heat. Mass.*, 2016, **77**, 49-53.
16. A. Jinich, B. Sanchez-Lengeling, H. Ren, R. Harman, et al., *ACS Cent. Sci.*, 2019, **5**, 1199-1210.
17. M. Jermyn, J. Desroches, J. Mercier, M. A. Tremblay, et al., *J. Biomed. Opt.*, 2016, **21**, 094002.
18. F. Lussier, D. Missirlis, J. P. Spatz and J. F. Masson, *ACS Nano*, 2019, **13**, 1403-1411.
19. F. Lussier, V. Thibault, B. Charron, G. Q. Wallace, et al., *Trac-Trend Anal. Chem.*, 2020, **124**, 115796.
20. C. Chen, N. Hayazawa and S. Kawata, *Nat. Commun.*, 2014, **5**, 3312.
21. N. Anderson, A. Hartschuh, S. Cronin and L. Novotny, *J. Am. Chem. Soc.* , 2005, **127**, 2533-2537.
22. S. Y. Moon and W. S. Kim, *Chem. Commun.*, 2019, **55**, 13888-13891.
23. C. Liu and H. Cheng, *J. Am. Chem. Soc.*, 2016, **138**, 6690-6698.
24. Y. Okuno, Y. Saito, S. Kawata and P. Verma, *Phys. Rev. Lett.*, 2013, **111**, 216101.
25. S. Chaunchaiyakul, T. Yano, K. Khoklang, P. Krukowski, et al., *Carbon*, 2016, **99**, 642-648.
26. N. Peica, C. Thomsen and J. Maultzsch, *Phys. Status Solidi B* 2010, **247**, 2818-2822.
27. N. Peica, C. Thomsen and J. Maultzsch, *Nanoscale Res. Lett.*, 2011, **6**, 174.
28. C. Georgi and A. Hartschuh, *Appl. Phys. Lett.*, 2010, **97**, 143117.
29. Y. Miyata, K. Mizuno and H. Kataura, *J. Nanomater.*, 2010, **2011**, 786763.
30. E. Sheremet, R. D. Rodriguez, A. L. Agapov, A. P. Sokolov, et al., *Carbon*, 2016, **96**, 588-593.
31. R. Rao, J. Reppert, R. Podila, X. Zhang, et al., *Carbon*, 2011, **49**, 1318-1325.
32. A. Bhattarai, K. T. Crampton, A. G. Joly, C.-F. Wang, et al., *J. Phys. Chem. Lett.*, 2020, **11**, 1915-1920.
33. S. D. M. Brown, A. Jorio, M. S. Dresselhaus and G. Dresselhaus, *Phys. Rev. B.*, 2001, **64**, 1-4.
34. E. Castillo-Martínez, J. Carretero-González, J. Sovich and M. D. Lima, *J. Mater. Chem. A*, 2014, **2**, 221-228.
35. H. Huang, R. Maruyama, K. Noda, H. Kajiura, et al., *J. Phys. Chem. B*, 2006, **110**, 7316-7320.
36. Z. Xu, Z. Liang and F. Ding, *Wires. Comput. Mol. Sci.*, 2017, **7**, e1283.
37. A. Jorio, M. A. Pimenta, A. G. S. Filho, R. Saito, et al., *New J. Phys.*, 2003, **5**, 139.
38. P. Puech, M. Kandara, G. Paredes, L. Moulin, et al., *C*, 2019, **5**, 69.
39. T. Yano, T. Ichimura, S. Kuwahara, F. H'Dhili, et al., *Nat. Commun.*, 2013, **4**, 2592.
40. M. S. Dresselhaus, G. Dresselhaus, R. Saito and A. Jorio, *Phys. Rep.*, 2005, **409**, 47-99.

